



Rugae-like Ni₂P-CoP nanoarrays as a bi-functional catalyst for hydrogen generation: NaBH₄ hydrolysis and water reduction

Jingya Guo^{a,1}, Benzhi Wang^{a,1}, Dandan Yang^a, Zixia Wan^a, Puxuan Yan^a, Jianniao Tian^a, Tayirjan Taylor Isimjan^{b,*}, Xiulin Yang^{a,*}

^a Guangxi Key Laboratory of Low Carbon Energy Materials, School of Chemistry and Pharmaceutical Sciences, Guangxi Normal University, Guilin, 541004, People's Republic of China

^b Saudi Arabia Basic Industries on (SABIC) at King Abdullah University of Science and Technology (KAUST) Saudi Arabia

ARTICLE INFO

Keywords:

Ni-Co₂₀-P arrays
Synergistic effect
NaBH₄ hydrolysis
Hydrogen evolution reaction

ABSTRACT

Designing a bifunctional catalyst that performs hydrolysis of metal hydrides and water reduction spontaneously is an essential step towards developing an integrated H₂ storage system. Herein, a series of rugae-like CoP-Ni₂P arrays decorated Ni foam (Ni-Co_x-P@NF) are fabricated by two-step electrodeposition followed by phosphating treatment. The optimized Ni-Co₂₀-P@NF catalyst shows a superior catalytic H₂ generation by NaBH₄ hydrolysis, giving a specific H₂ generation rate of 4323.0 mL min⁻¹ g⁻¹ catalyst and good reusability, far better than most previously reported catalysts. Besides, the catalyst also exhibits an excellent electrocatalytic hydrogen evolution reaction with a low overpotential of 67.0 mV to reach -10 mA cm⁻², small Tafel slope and long-term stability in 1.0 M KOH. The outstanding catalytic H₂ generation capacity is attributed to the synergistically catalytic effect between the Ni₂P and CoP species, as well as the unique composite structure with the benefit of solute transport and gas emission.

1. Introduction

Hydrogen (H₂) is clean energy sources that regarded as a future replacement of fossil fuel due to the highest energy per mass 142 MJ kg⁻¹ [1]. As an alternative of methane reforming, the electrochemical water splitting attracts a lot of attention due to the zero carbon emission and high purity H₂. Most importantly, H₂ can be generated using renewable energy such as solar and wind. However, the electrochemical water splitting requires a much higher voltage (1.8 ~ 2.0 V) than the theoretical limit of 1.23 V owing to the strong uphill reaction that requires high overpotentials [2]. As a result, it is critical to developing the efficient electrocatalysts that improve the sluggish kinetics thereof decrease the overpotential. The state-of-the-art hydrogen evaluation reaction (HER) catalysts are based on the expensive noble metal Pt [3,4]. Hence, extensive efforts have been devoted to developing robust and cheap noble-metal-free transition metal catalyst including sulfides, selenides, phosphides, carbides, and nitrides, etc. [5]. Among them, the increasing attention has been paid to metal phosphides (Ni₂P, CoP, MoP, and FeP) as HER catalyst because of the thermostability, high conductivity, and low cost [6]. Besides, the metal phosphides show bulk activity as compare to the metal sulfides of which the electrocatalytic

activity is limited to the edges [7]. Thus the metal phosphides often show better HER performance compare to those of others. Therefore, self-supported metal phosphide nanostructures *in situ* grown on 3D substrates have been widely exploited because the self-supported HER catalyst has several advantages as compared to a powder-based catalyst such as no binder, more active sites, better charge transfer and easy to be prepared [8–10]. However, the long term stability of the metal phosphides based HER catalyst is the primary concern.

Apart from the H₂ production, the H₂ storage is also a critical process for a sustainable “hydrogen economy”. H₂ storage is particularly challenging because of its low volumetric energy density. In general, there are two categories for storage H₂ including physical and chemical methods [11]. The physical storage based on forming either the high pressure (350 ~ 700 bar) compressed gas or low-temperature liquid. The hydrogen can also be stored on the surface of porous scaffolds through physical absorption, for example, organic frameworks and polymers with intrinsic porosity [12,13]. On the other hand, the chemical storage is realized by a reversible chemical bonding between hydrogen and absorbents including liquid organic (HCOOH) [14–16], interstitial metal hydride (LaNiH₆) [17], complex hydride (NaAlH₄) [18–20], and chemical hydride (NaBH₄) [21,22].

* Corresponding authors.

E-mail addresses: isimjant@sabic.com (T.T. Isimjan), xiulin.yang@kaust.edu.sa (X. Yang).

¹ These authors contributed equally.

However, developing high-density hydrogen storage for stationary and portable applications remains a significant challenge. Among all the chemical storage materials, chemical hydrides (NaBH_4 , NH_3BH_3 , and LiBH_4) are the best candidate in this regard because of the high hydrogen gravimetric storage capacity, stable chemical properties, and non-toxicity [23–25]. Nevertheless, boron hydride hydrolysis generally suffers from sluggish reaction kinetics. At present, platinum-based materials are the best performing catalysts for hydrolysis of sodium borohydride [26,27] and a lot of efforts have been made to develop the earth's abundant non-noble metal catalysts to replace the expensive platinum-based catalysts [28,29]. Among them, transition metal phosphides such as CoP/C nanoboxes [30], CoP₂ nanowire [31], Ni₂P@Ni-FeAlO_x [32], Ni – Cu – P nanotube [33], CoP/NiCoP [34], etc. become the hotspot. Wang et al. [35] and Zhang et al. [36] found that the bimetallic phosphides can significantly improve the catalytic performance as compared to single metal phosphides due to the synergistic effect. The maximum solubility of NaBH_4 in water is around 25 % therefore only a quarter of the NaBH_4 solution is consumed after NaBH_4 hydrolysis which means 75 % of the water is wasted.

Herein, we proposed a bifunctional Ni₂P-CoP catalyst that can be used spontaneously for NaBH_4 hydrolysis and HER catalyst (cathode) for water splitting. In another word, we can design a system that couples NaBH_4 hydrolysis with water splitting to maximize the H₂ extraction from both NaBH_4 and alkaline water solution. In this goal, we fabricated the rugae-like Ni₂P-CoP arrays decorated Ni foam catalyst by the integrating two-step electrodeposition followed by a vapor phase phosphatization. The optimized Ni-Co₂₀-P@NF exhibits an outstanding catalytic performances towards NaBH_4 hydrolysis and HER in two separate system. Moreover, it also shows excellent reusability and long-term stability. The superior H₂ production capacity can be explained by the following two aspects including the hierarchical porous structures resulted in abounded active sites and better mass transfer [37] as well as the synergetic effect between Ni₂P and CoP species [38].

2. Experimental section

2.1. Synthesis of Ni-Co_x-species@NF

All chemicals are analytical grade and do not require further purification in experiments. Firstly, pretreatment of the nickel foam (1 cm × 1 cm × 1.6 mm) with 1.0 M HCl, deionized water and ethanol for 5 min respectively, and then repeated 3 times to make sure the surface of the NF was well cleaned. To prepare the Ni-Co-species@NF, 1.0 mmol of $\text{Co}(\text{NO}_3)_2 \cdot 6\text{H}_2\text{O}$ and 1.0 mmol of $\text{Ni}(\text{NO}_3)_2 \cdot 6\text{H}_2\text{O}$ was ultrasonically dissolved into 40 mL deionized water to form uniform solutions, respectively. The electrodeposition experiments were carried out at room temperature in a standard three-electrode system to electrodeposit Co-species and Ni-species in sequence. The NF skeleton was used as the working electrode, a Pt sheet and a saturated calomel electrode SCE electrode used as the counter electrode and the reference electrode respectively. A series of composites with different Co/Ni molar ratios were synthesized by changing the deposition times at a constant current density of -10 mA cm^{-2} , in which the total electrodeposition time is kept at 1.0 h. After being thoroughly washed and dried at room temperature, the resulted products were labeled as Ni-Co_x@NF (x = 5, 10, 15, 20 and 25).

We prepared a series of control materials by changing one parameter at a time. First, the order of electrodeposition of Co/Ni was reversed, while the ratio of Ni/Co was kept at 1/20 (Co₂₀-Ni@NF). Second, a mixture of Ni-Co solution was prepared with the molar ratio of Ni/Co for 1/20 [(Co₂₀Ni)@NF]. Third, only Co or Ni species was electrodeposited on the surface of NF (Co@NF and Ni@NF). All of the above experiments were performed at -10 mA cm^{-2} for a total deposition time of 1.0 h.

2.2. Synthesis of Ni-Co_x-P@NF by vapor phase phosphidation

The phosphidation process was performed in a tube furnace, where a porcelain boat containing NaH_2PO_2 as a phosphorus source was placed upstream, and all electrodeposited products were placed in another porcelain boat placed downstream. The furnace was heated to 350 °C with 2 °C min⁻¹ in Ar atmosphere (20 sccm), and kept at 350 °C for 2 h. After the phosphidation, the samples were cooled down to ambient temperature in flowing Ar gas. Thereafter, a series of samples were prepared and named as Ni-Co_x-P@NF (x = 5, 10, 15, 20 and 20), Co₂₀-Ni-P@NF, (Co₂₀Ni)P@NF, CoP@NF and Ni₂P@NF, etc., as the following studies.

As a control, commercial Pt/C modified NF was also prepared, where 10.0 mg of commercial 20 wt% Pt/C powder was ultrasonically dispersed in 0.5 ml of 0.2 wt% Nafion solution. After 30 min, the resulted mixture was pipetted onto the surface of NF (1 cm × 1 cm) and dried naturally in air.

2.3. Characterizations

The crystal structures of catalysts were analyzed by X-ray powder diffraction (XRD, Rigaku D/Max 2500 V/PC) with a sweep speed for 2.0 ° min⁻¹. The morphologies and microstructures of the catalysts were characterized by scanning electron microscope (SEM, FEI Quanta 200 FEG) and transmission electron microscope (TEM, JEM-2100 F). The X-ray photoelectron spectrometer (XPS, JPS-9010 Mg Kα) was used to analyze the chemical states of different elements. The actual loadings of different metals in the catalyst were checked by inductive coupled plasma atomic emission spectroscopy (ICP-AES, IRIS Intrepid II XSP). The specific BET surface area of the as-prepared materials were measured on Quantachrome instrument. The conductivity of various materials were tested by four-point probe meter (RTS-9).

2.4. Catalytic hydrolysis of sodium borohydride studies

The catalytic activity, cycle stability and activation energy of the catalytic material were obtained by the following methods. Typically, 50 mL mixture solution (contained 150 mM NaBH_4 + 0.4 wt% NaOH) was kept in a three-necked round-bottom flask (100 mL), which was placed in a water bath at 25 °C. The volume of H₂ was monitored by a drainage which was connected to a computer to record the instantly changed water quantity. The catalytic reaction was started when the catalyst was added into the flask under constant magnetic stirring conditions. In order to test the recyclability of the catalyst, we continued to use the fresh NaBH_4 solution instead of the fully decomposed NaBH_4 solution for five consecutive cycles at 25 °C. After each stability test, we centrifuged the catalytic material, dried it under vacuum condition at room temperature, and weighed the catalytic material. All experiments were repeated three times to ensure the reliable results. The activation energy of the designed catalyst was evaluated in the same device in the temperature range of 25–45 °C.

2.5. Electrochemical hydrogen evolution studies

The electrocatalytic performance of different catalysts were performed in a standard three-electrode system with a Multi-channel electrochemical workstation (Bio-logic VMP3, France) at room temperature. The graphite plate and a saturated calomel electrode (SCE) were used as counter and reference electrodes, respectively. Cyclic voltammetry (CV) tests were firstly carried out for about 3–5 cycles to stabilize the electrocatalytic performance of the catalyst at a scan rate of 20 mV s⁻¹. Then, liner sweep voltammetry (LSV) curves were performed at a scan rate of 5 mV s⁻¹, and electrochemical impedance spectroscopy (EIS) was evaluated near the onset potential in the frequency range from 200 kHz to 10 mHz. Cyclic voltammetry (CV) method was used to derive the electrochemical double-layer

capacitance (C_{dl}) in a non-Faradaic potential window. The electrochemical double-layer is similar to the regular capacitors where the energy stored in the C_{dl} by simply charge separation. Therefore, the stored energy can be calculated using the conventional capacitor equation [39]: $Q = C_{dl}V = \frac{\epsilon \epsilon_0 A V^2}{d}$, where V is voltage, A is electrochemically active surface area, d distance between two layers, and ϵ is the permittivity of the dielectric. Therefore, the C_{dl} is directly proportional to the electrochemically active surface area (EASA) of the electrocatalysts. All potentials (vs. SCE) in this work were calibrated to the RHE by the average CV curves of the two potentials at which the current crossed zero (1.044 V) was taken to be the thermodynamic potential in H_2 -saturated 1.0 M KOH. Two clean Pt sheets are used as the working and counter electrodes in the calibration system, respectively. All reported curves had been corrected by iR compensation and all the electrochemical tests were performed at room temperature (25 ± 1 °C).

3. Results and discussion

The Ni-Co_x-P@NF materials were fabricated by consecutive three steps, in which Co-species were first electrodeposited onto the surface of NF to form Co-species nanosheet arrays. Thereafter, the Ni species were subsequently electrodeposited onto the surface of the Co-species nanosheet arrays. Finally, after the gas phase phosphating treatment, a series of the target Ni-Co_x-P@NF composites with different Co/Ni ratios were prepared (Fig. 1a). The XRD patterns were adopted to explore the changes in crystal structure of the catalytic materials. Fig. S1a–b shows that the prepared Co-species and Ni-species on the NF surface are consistent with the standard XRD patterns of Co(OH)₂ (JCPDS: 30-0443) and Ni(OH)₂ (JCPDS: 38-0715), respectively. The Co and Ni were electrochemically deposited on the NF where they are in the metallic state initially, but they are subsequently oxidized in the air to Co(OH)₂ and Ni(OH)₂. After phosphating, the pure Ni-species on NF surface is subsequently converted to Ni₂P (JCPDS: 03-0953), while the Co-species are transformed to CoP (JCPDS: 65-2593) (Fig. 1b). The XRD patterns of Ni-Co₂₀-P@NF is dominated by the CoP peaks indicating the low-content of Ni₂P in the hybrid composite. This phenomenon was simultaneously observed in the series of Ni-Co_x-P@NF and Co₂₀-Ni-P@NF materials (Fig. S1c). However, the XRD pattern of (Co₂₀Ni)P@NF

obtained by electroplating at the same time shows strong Ni₂P diffraction peaks because more Ni species are electrodeposited on NF surface due to the higher standard reduction potentials of Ni²⁺ (-0.23 V) than Co²⁺ (-0.28 V) under the same conditions (Fig. S1d).

SEM and TEM are used to investigate the morphologies and nanostructure of the catalysts. Fig. 2a shows that the fresh NF has a three-dimensional structure and the surface is very smooth. After electro-deposition of Co-species and phosphatization, the resulted rugae-like CoP nanosheet arrays are vertically distributed on the surface of the NF (Fig. S2a). It is worth noting that when the Co/Ni ratio is less than 10/1, a large amount of Ni₂P clusters appear on the surface of CoP nanosheets (Fig. S2b–c), and as the Co/Ni ratio increases, the observed Ni₂P clusters gradually decrease (Fig. 2b and Fig. S2d–e). Interestingly, the Co/Ni ratios have little effect on the overall morphologies of Ni-Co_x-P@NF composites, except for the partial agglomeration of pure Ni₂P on NF (Fig. S2f). As a control, the Co₂₀-Ni-P material presented irregular morphology on the surface of NF at a high magnification SEM images and was mainly composed by a large number of particulate materials (Fig. S2g). Notably, the large spacings between these nano-sheets facilitate the mass transfer, thereby increasing in catalytic activity. The TEM image of the ultrasonically exfoliated Ni-Co₂₀-P nanosheets reveals that the Ni₂P clusters are uniformly distributed on the surface of CoP with an average diameter of 6.0 nm (Fig. 2c). The high-resolution TEM image shows a set of lattice spacings of 0.25 and 0.19 nm, corresponding to the (111) and (211) crystal planes of CoP, respectively. The other set of lattice spacings is 0.20 and 0.19 nm, which correspond to the (201) and (210) crystal planes of Ni₂P, respectively (Fig. 2d). Furthermore, the HAADF-STEM and corresponding element mappings demonstrate that the elements of Co, Ni and P are uniformly dispersed the entire architectures of Ni-Co₂₀-P@NF (Fig. 2e).

Moreover, the specific surface areas of Ni-Co₂₀-P@NF, Co₂₀-Ni-P@NF and CoP@NF were investigated by Brunauer–Emmett–Teller (BET) gas-sorption measurements (Fig. S3). The results reveal that the BET surface area of Ni-Co₂₀-P@NF is 18.2 m² g⁻¹, which is ca. 1.57- and 2.60-fold higher than that of Co₂₀-Ni-P@NF and CoP@NF, respectively. Interestingly, the Ni-Co₂₀-P@NF also shows a high conductivity (2703 S cm⁻¹), which is ca. 2.92-, 1.46- and 2.76-times larger than that of Co₂₀-Ni-P@NF, CoP@NF and Ni₂P@NF, respectively (Table S1). It is known that the high BET surface area helps to expose more active sites and large conductivity enhances electron transport, an improved catalytic performance is expected.

X-ray photoelectron spectroscopy (XPS) was used to further study the changes in the surface chemical states of the composites and associated electron transfer properties. As shown in Fig. S4a–b, the Ni-Co₂₀-P@NF material is composed of C, O, Co, Ni and P elements, in which the high-resolution C1s region is deconvoluted into C–C (284.8 eV), CO (286.0 eV) and CO= (288.7 eV) as standard corrections for other elements [40]. The Co 2p region of Ni-Co₂₀-P@NF contains a pair of Co 2p_{3/2} and Co 2p_{1/2}, where the Co 2p_{3/2} is fitted into three peaks of Co–P (779.2 eV), CoO– (782.4 eV) and a satellite (786.4 eV), respectively (Fig. 3a). Compared to CoP@NF, the binding energy of Co–P of Ni-Co₂₀-P@NF is positively shifted by 0.82 eV. Besides, the Ni 2p_{3/2} region of Ni-Co₂₀-P@NF is also fitted with three peaks of Ni–P (854.7 eV), Ni–O (857.8 eV) and one satellite peak (862.8 eV). Contrary to Co 2p, the binding energy of the Ni–P of Ni-Co₂₀-P@NF is negatively shifted by 0.47 eV as compared to that of Ni₂P@NF (Fig. 3b). It is worth noting that we have also studied the high-resolution Co 2p and Ni 2p of Ni-Co₁₅-P@NF and Ni-Co₂₅-P@NF, and observed that they have a similar chemical states distribution with Ni-Co₂₀-P@NF (Fig. S4c–d). Besides, the P 2p of Ni-Co₂₀-P@NF is fitted in Fig. 3c, where the high-resolution P 2p mainly includes P 2p_{3/2} (130.6 eV) and P 2p_{1/2} (131.7 eV) of Co–P or NiP, and additional PO= bonds (134.7 eV). One should note that the positive shift on the Co–P and the negative shift on the Ni–P binding energies in the Ni-Co₂₀-P@NF indicates the charge transfer from the CoP species to the Ni₂P species [41], implying the synergy between CoP and Ni₂P species.

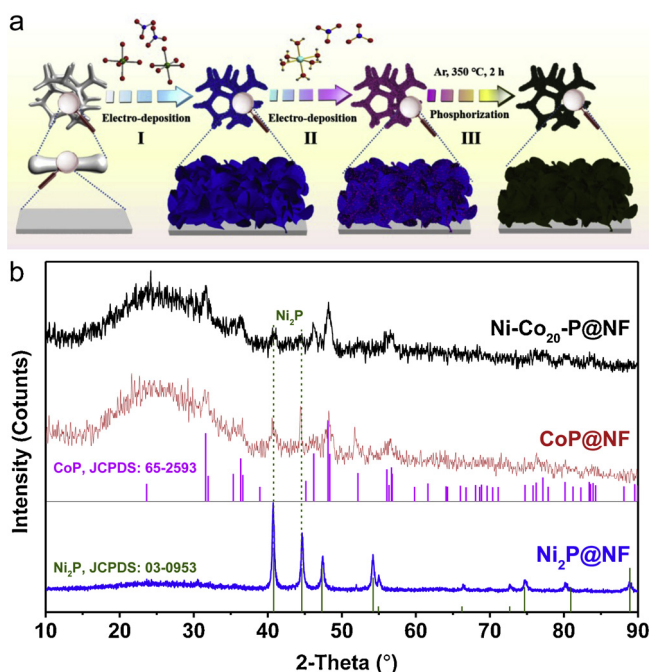


Fig. 1. (a) Schematic diagram of the formation of Ni-Co₂₀-P@NF catalyst. (b) X-ray diffraction (XRD) patterns of Ni-Co₂₀-P@NF, CoP@NF and Ni₂P@NF.

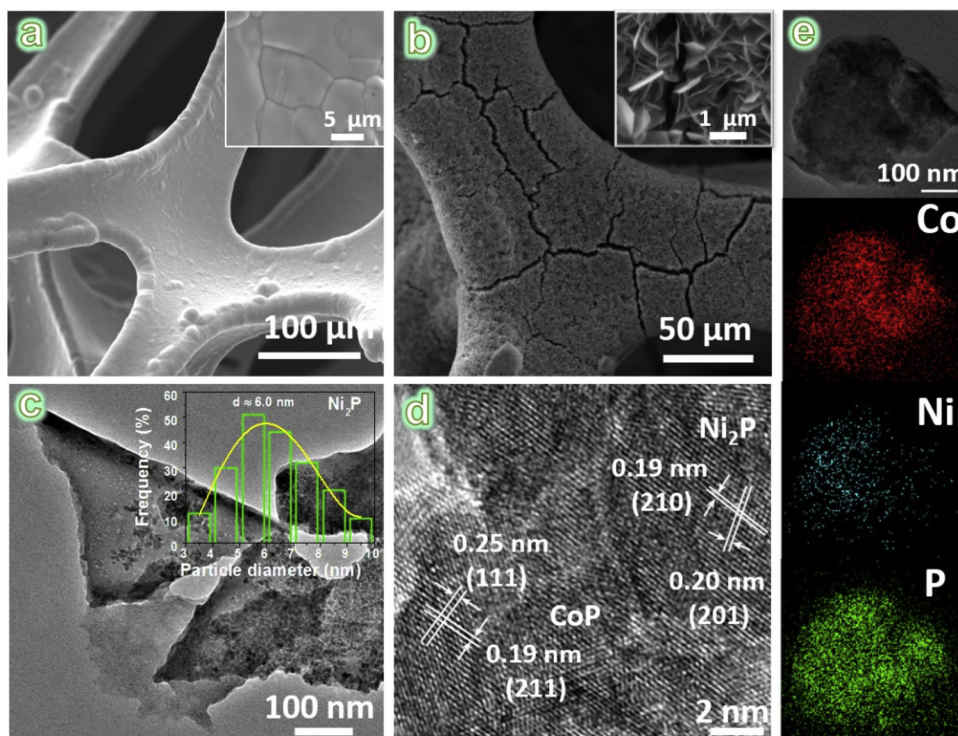


Fig. 2. Scanning electron microscopy (SEM) images of (a) NF, (b) Ni-Co₂₀-P@NF. The insets are the magnified SEM images. (c) Transmission electron microscopy (TEM) and (d) high-resolution TEM images of Ni-Co₂₀-P@NF.

The catalytic hydrolysis of NaBH₄ for H₂ generation is carried out in an alkaline environment at 25 °C, wherein the generated H₂ gas is calculated by weighing the water mass produced by the drainage method (Fig. S5). Firstly, we explored the effect of Ni-Co₂₀-P@NF catalysts prepared by different ratios of Co/Ni on H₂ production by catalytic hydrolysis. It can find that the catalytic hydrolysis performance begins to increase gradually until the ratio for 20/1 and then decreases slightly with the increase of Co contents (Fig. 4a). When the ratio of Co/Ni is 20/1, the maximum catalytic hydrolysis H₂ generation rate is 4323.0 mL min⁻¹ g⁻¹ (Fig. 4b), wherein the calculated mass (g) is the total mass of Co and Ni, which is obtained by ICP test. To eliminate the influence of nickel form on the actual Co/Ni molar ratio, the carbon cloth (CC) was used as the support and prepared a series of Ni-Co_x-P modified CC composites. To monitor the Ni loading effect, the Ni loading was started from very low to high. The ICP-AES results were

consistent with the original design, as shown in Tables S2 and S3. The Ni-Co₂₀-P@NF showed better catalytic performance than that of Co₂₀-Ni-P@NF on NaBH₄ hydrolysis due to the following reasons. Firstly, the catalyst of CoP is a much better catalyst than Ni₂P in terms of NaBH₄ hydrolysis [42,43]. Moreover, CoP@NF shows well-orientated nanosheet array structure as compare to that of the disorientated Ni₂P@NF where CoP@NF not only has better coverage but also offers higher surface area for Ni to attach (Fig. S3). The SEM images of both Ni-Co₂₀-P@NF and Co₂₀-Ni-P@NF reveal the same fact as a Ni₂P clusters decorated CoP@NF vs an irregular Co₂₀-Ni-P@NF morphology (Fig. S2). More surface area means more active sites as shown in Fig. 6c where the electrochemical capacitance (C_{dl}) of Ni-Co₂₀-P@NF is almost 1.82-fold higher than that of Co₂₀-Ni-P@NF which is directly proportional to the number of active sites [44,45]. Secondly, we explored the effects of different types of catalysts on the catalytic H₂ generation, in which the

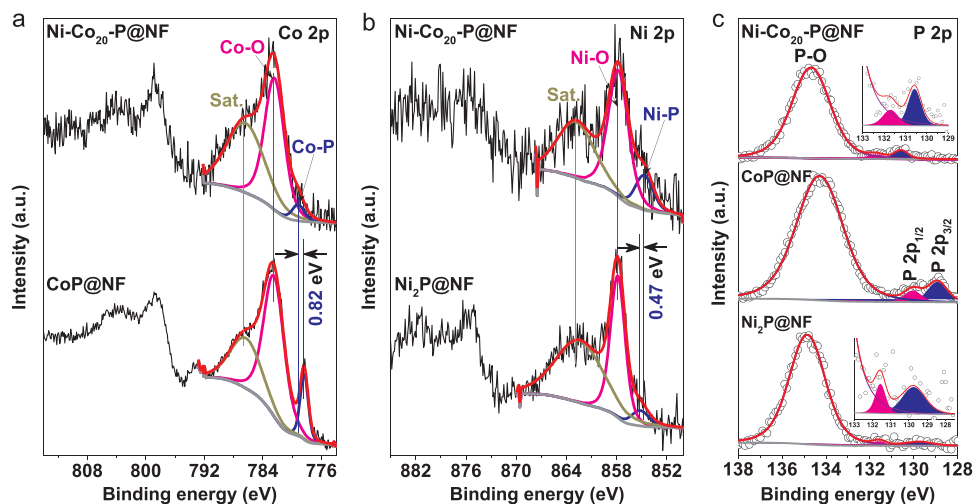


Fig. 3. High-resolution XPS spectra of (a) Co 2p, (b) Ni 2p and (c) P 2p regions of Ni-Co₂₀-P@NF, CoP@NF and Ni₂P@NF, respectively.

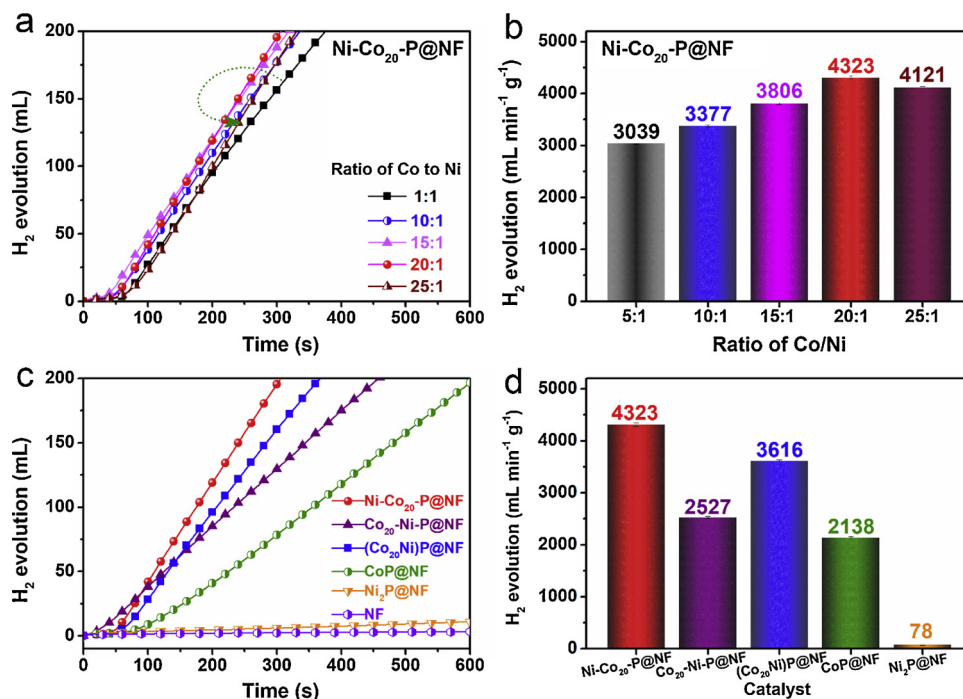


Fig. 4. (a) Stoichiometric H₂ evolution in 150 mM NaBH₄ + 0.4 wt % NaOH solution by Ni-Co₂₀-P@NF catalysts with different ratios of Co/Ni at 25 °C, and (b) the corresponding H₂ evolution rate values. (c) H₂ evolution by different catalysts at 25 °C, and (d) the summarized H₂ evolution rate values.

Ni-Co₂₀-P@NF catalyst still showed the best catalytic performance compared with the control catalysts prepared by different methods (Fig. 4c). We can see that the H₂ generation rate of Ni-Co₂₀-P@NF catalyst is approximate 1.71-, 1.20-, 2.02- and 55.42-fold higher than those of Co₂₀-Ni-P@NF, (Co₂₀Ni)P@NF, CoP@NF and Ni₂P@NF, respectively (Fig. 4d). Meanwhile, the high catalytic H₂ generation rate is also superior to most of the previously reported catalysts (Table S4). Such excellent catalytic activity is mainly caused by the synergistic effect between CoP and Ni₂P species combined with more catalytically active sites.

The temperature effect to the catalytic performance of Ni-Co₂₀-P@

NF and CoP@NF in the alkalinized NaBH₄ solution are further investigated (Fig. 5a and Fig. S6). The results revealed that the catalytic performance increases with the increasing reaction temperatures. Moreover, the activation energies of Ni-Co₂₀-P@NF and CoP@NF are estimated to be 30.1 kJ mol⁻¹ and 56.1 kJ mol⁻¹ [40] respectively, and the activation energy of Ni-Co₂₀-P@NF is almost half of the that of CoP@NF (Fig. 5b) once again implies the strong positive synergy between Co and Ni species in the Ni-Co₂₀-P@NF. The reusability of Ni-Co₂₀-P@NF catalyst was evaluated by the continuous recycling experiments in alkalinized NaBH₄ solution. The results show that it takes 5–8 min to collect 200 mL of H₂ from the 1st to the 5th use (Fig. 5c) as

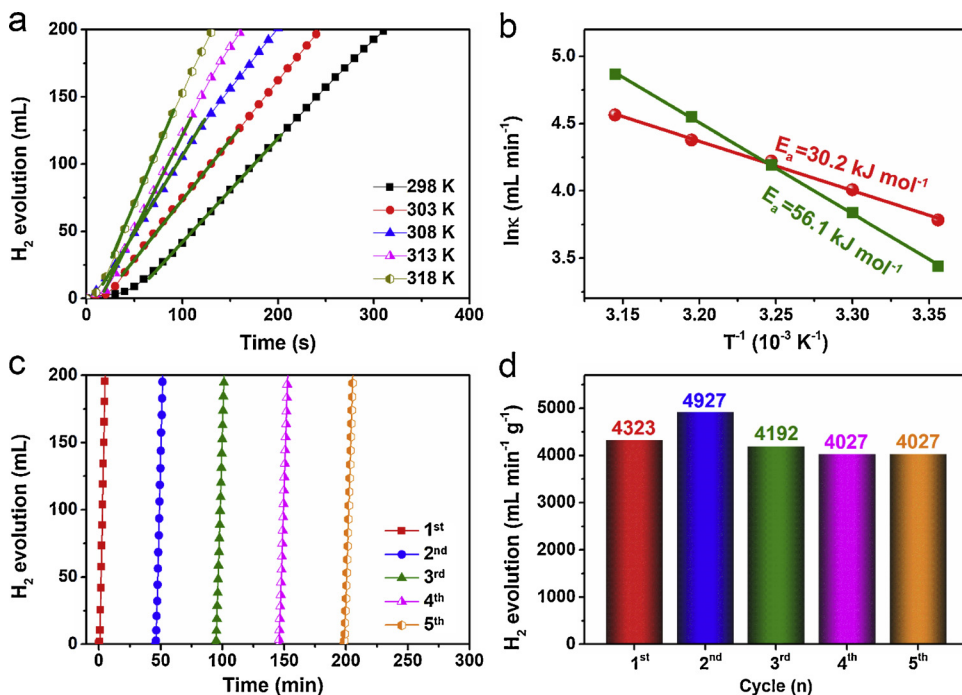


Fig. 5. (a) The relationship between the H₂ generation rate and applied temperatures of Ni-Co₂₀-P@NF. (b) The summarized Arrhenius plots for Ni-Co₂₀-P@NF and CoP@NF. (c) Recycling stability test of Ni-Co₂₀-P@NF catalyst in 150 mM NaBH₄ + 0.4 wt % NaOH at 25 °C. (d) The summarized specific H₂ generation rates in the different recycling test.

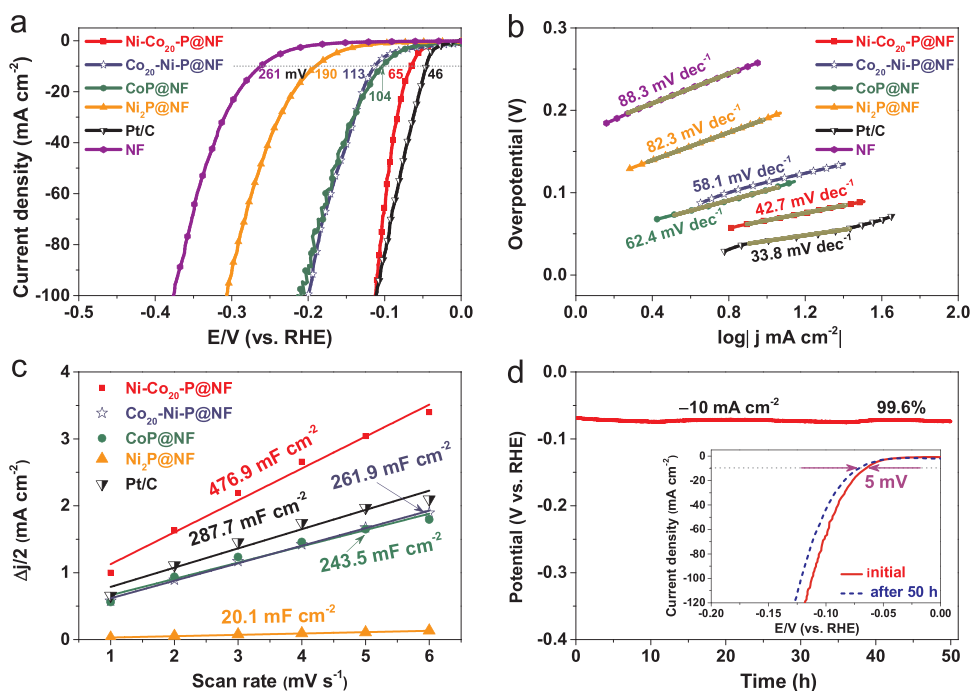


Fig. 6. (a) Polarization curves and (b) Tafel plots of Ni-Co₂₀-P@NF, Co₂₀-Ni-P@NF, CoP@NF, Ni₂P@NF, Pt/C and NF. All the measurements are carried out in 1.0 M KOH at a scan rate of 2 mV s⁻¹. (c) The summarized double-layer capacitance (C_{dl}) of different catalysts. (d) Chronopotentiometric curve of Ni-Co₂₀-P@NF catalyst at -10 mA cm⁻² for 50 h. Inset is the LSV curves before and after the stability test.

shown in Fig. 5d, the Ni-Co₂₀-P@NF catalyst showed a good recyclability and retained 92 % of initial catalytic activity after 5th cycle. The slight decay of catalytic activity could be attributed to the exfoliation of the catalytic materials and catalyst poisoning by BO₂⁻ species [23,46].

In addition to the catalytic hydrolysis of NaBH₄, the HER performance of the Ni-Co_x-P@NF is also measured in 1.0 M KOH solution. All the HER results are corrected to the RHE potential, and the calibration parameter is obtained in an H₂ saturated electrolyte (Fig. S7). We first studied the Ni-Co_x-P@NF catalyst with different Co/Ni ratios and found that the HER catalytic activity increased with the increasing Co contents to reach the maximum at 20/1, and then decreased gradually (Fig. S8a). Similar to the NaBH₄ hydrolysis results, the Co/Ni ratio of 20/1 shows the best HER performance meaning it has the lowest overpotential, the smallest Tafel slope (Fig. S8b), the highest double-layer capacitance (C_{dl}, Fig. S8c and Fig. S9), and the lowest charge transfer resistance (R_{ct}, Fig. S8d). Subsequently, we used the polarization curves of different catalysts to evaluate their catalytic activity (Fig. 6a). Nyquist plots of the catalysts reveal that the R_{ct} of Ni-Co₂₀-P@NF is the smallest among all other catalysts indicating the fastest electrocatalytic reaction rate (Fig. S10) [47]. Among them, the optimized Ni-Co₂₀-P@NF catalyst only required an overpotential of 65 mV to reach a current density of -10 mA cm⁻², far better than the control catalysts of CoP@NF, Ni₂P@NF and NF, and most of the previously reported catalysts (Table S5).

The Tafel slope gives insights into the rate-determining step in the HER process [48]. The Tafel slopes of Ni-Co₂₀-P@NF, CoP@NF, Ni₂P@NF, Pt/C@NF, and NF catalysts are calculated to be 42.7, 62.4, 82.3, 33.8 and 88.3 mV dec⁻¹, respectively (Fig. 6b). These Tafel slope values are mainly between 40 and 120 mV dec⁻¹ except Pt/C@NF catalyst, suggesting they follow the Volmer-Heyrovsky mechanism and (H_{ads} + H₂O + e⁻ → H₂ + OH⁻) is the rate-limiting step [49]. Because the electrocatalytic activity of a given material scales with its exposed area [50], which, in turn, can be correlated to the double layer capacitance (C_{dl}) at the solid-liquid interface. To measure the C_{dl}, the non-Faradaic potential windows are selected to operate CV cycles with different scan rates (1~6 mV s⁻¹) (Fig. S11). The resulted current densities plotted against scan rates are shown in Fig. 6c. The C_{dl} of Ni-Co₂₀-P@NF is computed equal to 476.9 mF cm⁻², which is significantly higher than those of the Co₂₀-Ni-P@NF (261.9 mF cm⁻²),

CoP@NF (243.5 mF cm⁻²), Ni₂P@NF (20.1 mF cm⁻²) and Pt/C@NF (287.7 mF cm⁻²). These results indicate that the Ni-Co₂₀-P@NF has the largest electrochemical active surface area compared to the rest.

The electrochemical stability of Ni-Co₂₀-P@NF catalyst was explored under a constant current density (-10 mA cm⁻²) in 1.0 M KOH solution (Fig. 6d). We found that the catalyst shows almost no degradation even after 50 h of continuous running, indicating excellent electrochemical stability. We also compared the LSV polarization curves before and after the long-term stability, where the overpotential of the Ni-Co₂₀-P@NF catalyst decayed by ca. 5 mV after the stability test at the current density of -10 mA cm⁻² (Inset of Fig. 6d). This superior electrochemical stability is believed to be associated with a unique preparation process that effectively reduces the voids between the catalyst and the support, thereby avoiding catalyst exfoliation and increasing electron conductivity.

4. Conclusion

In summary, a high-performance bifunctional catalyst of the rugae-like Ni₂P-CoP arrays decorated NF is fabricated by a two-step electro-deposition plus a vapor phase phosphatization treatment. The XRD patterns and SEM images have characterized the crystal structures and morphologies, and the TEM image shows that the Ni₂P nanoclusters are distributed on the surface of the CoP nanosheet arrays with an average size of ca. 6 nm. The XPS spectra indicate that there is a substantial charge transfer between CoP and Ni₂P in Ni-Co₂₀-P@NF composite. The H₂ generation by catalytic NaBH₄ hydrolysis shows that the optimized Ni-Co₂₀-P@NF catalyst has a higher H₂ evolution rate (4323.0 mL min⁻¹ g⁻¹) and is higher than most of the previously reported non-precious metal catalysts. Besides, the Ni-Co₂₀-P@NF catalyst also demonstrates excellent electrocatalytic H₂ production capacity with low overpotential (65 mV) to reach 10 mA cm⁻², small Tafel slope (42.7 mV dec⁻¹), and high double layer capacitance (476.9 mF cm⁻²). Also, the Ni-Co₂₀-P@NF catalyst exhibits excellent reusability and long-term stability, presenting a potential commercial application.

Declaration of Competing Interest

The authors declare that they have no known competing financial

interests or personal relationships that could have appeared to influence the work reported in this paper.

Acknowledgements

This work has been supported by the National Natural Science Foundation of China (no. 21965005), Natural Science Foundation of Guangxi Province (2018GXNSFAA294077), Project of High-Level Talents of Guangxi (F-KA18015, 2018ZD004) and Innovation Project of Guangxi Graduate Education (XYCSZ2019056, YCBZ2019031).

Appendix A. Supplementary data

Supplementary material related to this article can be found, in the online version, at doi:<https://doi.org/10.1016/j.apcatb.2019.118584>.

References

- [1] P. Brack, S.E. Dann, K.G.U. Wijayantha, P. Adcock, S. Foster, An old solution to a new problem? Hydrogen generation by the reaction of ferrosilicon with aqueous sodium hydroxide solutions, *Energy Sci. Eng.* 3 (2015) 535–540.
- [2] L. Shao, H. Sun, L. Miao, X. Chen, M. Han, J. Sun, S. Liu, L. Li, F. Cheng, J. Chen, Facile preparation of NH₂-functionalized black phosphorene for the electrocatalytic hydrogen evolution reaction, *J. Mater. Chem. A* 6 (2018) 2494–2499.
- [3] Y. Shi, B. Zhang, Recent advances in transition metal phosphide nanomaterials: synthesis and applications in hydrogen evolution reaction, *Chem. Soc. Rev.* 45 (2016) 1529–1541.
- [4] Y. Zheng, Y. Jiao, A. Vasileff, S.Z. Qiao, The hydrogen evolution reaction in alkaline solution: from theory, single crystal models, to practical electrocatalysts, *Angew. Chem. Int. Ed.* 57 (2018) 7568–7579.
- [5] H. Sun, Z. Yan, F. Liu, W. Xu, F. Cheng, J. Chen, Self-supported transition-metal-based electrocatalysts for hydrogen and oxygen evolution, *Adv. Mater.* (2019) 1806326, <https://doi.org/10.1002/adma.201806326>.
- [6] H. Du, R.-M. Kong, X. Guo, F. Qu, J. Li, Recent progress in transition metal phosphides with enhanced electrocatalysis for hydrogen evolution, *Nanoscale* 10 (2018) 21617–21624.
- [7] E.J. Popczun, J.R. McKone, C.G. Read, A.J. Biacchi, A.M. Wiltout, N.S. Lewis, R.E. Schaak, Nanostructured nickel phosphide as an electrocatalyst for the hydrogen evolution reaction, *J. Am. Chem. Soc.* 135 (2013) 9267–9270.
- [8] F. Jing, Q. Lv, Q. Wang, K. Chi, Z. Xu, X. Wang, S. Wang, Self-supported 3D porous N-doped nickel selenide electrode for hydrogen evolution reaction over a wide range of pH, *Electrochim. Acta* 304 (2019) 202–209.
- [9] X. Lv, Z. Hu, J. Ren, Y. Liu, Z. Wang, Z.-Y. Yuan, Self-supported Al-doped cobalt phosphide nanosheets grown on three-dimensional Ni foam for highly efficient water reduction and oxidation, *Inorg. Chem. Front.* 6 (2019) 74–81.
- [10] C. Sun, J. Zeng, H. Lei, W. Yang, Q. Zhang, Direct electrodeposition of phosphorus-doped nickel superstructures from choline chloride–Ethylene glycol deep eutectic solvent for enhanced hydrogen evolution catalysis, *ACS Sustain. Chem. Eng.* 7 (2018) 1529–1537.
- [11] U.B. Demirci, About the technological readiness of the H₂ generation by hydrolysis of B(–N)–H compounds, *Energy Technol.* 6 (2018) 470–486.
- [12] A. Indra, T. Song, U. Paik, Metal organic framework derived materials: progress and prospects for the energy conversion and storage, *Adv. Mater.* 30 (2018) 1705146.
- [13] D.-X. Xue, Q. Wang, J. Bai, Amide-functionalized metal–organic frameworks: syntheses, structures and improved gas storage and separation properties, *Coord. Chem. Rev.* 378 (2019) 2–16.
- [14] N. Onishi, G. Laurenczy, M. Beller, Y. Himeda, Recent progress for reversible homogeneous catalytic hydrogen storage in formic acid and in methanol, *Coord. Chem. Rev.* 373 (2018) 317–332.
- [15] K. Sordakis, C. Tang, L.K. Vogt, H. Junge, P.J. Dyson, M. Beller, G. Laurenczy, Homogeneous catalysis for sustainable hydrogen storage in formic acid and alcohols, *Chem. Rev.* 118 (2018) 372–433.
- [16] M. Niermann, A. Beckendorff, M. Kaltschmitt, K. Bonhoff, Liquid Organic Hydrogen Carrier (LOHC)–Assessment based on chemical and economic properties, *Int. J. Hydrogen Energy* 44 (2019) 6631–6654.
- [17] R. Zacharia, S. Rather, Review of solid state hydrogen storage methods adopting different kinds of novel materials, *J. Nanomater.* 2015 (2015) 1–18.
- [18] L. Li, C. Xu, C. Chen, Y. Wang, L. Jiao, H. Yuan, Sodium alanate system for efficient hydrogen storage, *Int. J. Hydrogen Energy* 38 (2013) 8798–8812.
- [19] E. Ianni, M.V. Sofianos, M.R. Rowles, D.A. Sheppard, T.D. Humphries, C.E. Buckley, Synthesis of NaAlH₄/Al composites and their applications in hydrogen storage, *Int. J. Hydrogen Energy* 43 (2018) 17309–17317.
- [20] R. Palm, H. Kurig, J. Aruväli, E. Lust, NaAlH₄/microporous carbon composite materials for reversible hydrogen storage, *Microporous Mesoporous Mater.* 264 (2018) 8–12.
- [21] J. Mao, D. Gregory, Recent advances in the use of sodium borohydride as a solid state hydrogen store, *Energies* 8 (2015) 430–453.
- [22] U.B. Demirci, Impact of H.I. Schlesinger's discoveries upon the course of modern chemistry on B(–N)–H hydrogen carriers, *Int. J. Hydrogen Energy* 42 (2017) 21048–21062.
- [23] J. Guo, C. Wu, J. Zhang, P. Yan, J. Tian, X. Shen, T.T. Isimjan, X. Yang, Hierarchically structured rugae-like RuP₃–CoP arrays as robust catalysts synergistically promoting hydrogen generation, *J. Mater. Chem. A* 7 (2019) 8865–8872.
- [24] L. Ouyang, W. Chen, J. Liu, M. Felderhoff, H. Wang, M. Zhu, Enhancing the re-generation process of consumed NaBH₄ for hydrogen storage, *Adv. Energy Mater.* 7 (2017) 1700299.
- [25] L. Cui, Y. Xu, L. Niu, W. Yang, J. Liu, Monolithically integrated CoP nanowire array: an on/off switch for effective on-demand hydrogen generation via hydrolysis of NaBH₄ and NH₃BH₃, *Nano Res.* 10 (2016) 595–604.
- [26] B. Li, L. Jiang, X. Li, Z. Cheng, P. Ran, P. Zuo, L. Qu, J. Zhang, Y. Lu, Controllable synthesis of nanosized amorphous MoS₂ using temporally shaped femtosecond laser for highly efficient electrochemical hydrogen production, *Adv. Funct. Mater.* 29 (2019) 1806229.
- [27] X. Cheng, D. Wang, J. Liu, X. Kang, H. Yan, A. Wu, Y. Gu, C. Tian, H. Fu, Ultra-small Mo₂N on SBA-15 as high-efficient promoter of low-loading Pd for catalytic hydrogenation, *Nanoscale* 10 (2018) 22348–22356.
- [28] L.B. Huang, L. Zhao, Y. Zhang, Y.Y. Chen, Q.H. Zhang, H. Luo, X. Zhang, T. Tang, L. Gu, J.S. Hu, Self-Limited on-Site Conversion of MoO₃Nanodots into Vertically Aligned Ultrasmall Monolayer MoS₂ for Efficient Hydrogen Evolution, *Adv. Energy Mater.* 8 (2018) 1800734.
- [29] W. Ahn, G. Park Moon, U. Lee Dong, H. Seo Min, G. Jiang, P. Cano Zachary, M. Hassan Fathy, Z. Chen, Hollow multivoid nanocuboids derived from ternary Ni-Co-Fe prussian blue analog for dual-electrocatalysis of oxygen and hydrogen evolution reactions, *Adv. Funct. Mater.* 28 (2018) 1802129.
- [30] X. Wang, Z. Na, D. Yin, C. Wang, Y. Wu, G. Huang, L. Wang, Phytic acid-assisted formation of hierarchical porous CoP/C nanoboxes for enhanced Lithium storage and hydrogen generation, *ACS Nano* 12 (2018) 12238–12246.
- [31] Y. Zhou, Y. Yang, R. Wang, X. Wang, X. Zhang, L. Qiang, W. Wang, Q. Wang, Z. Hu, Rhombic porous CoP₂ nanowire arrays synthesized by alkaline etching as highly active hydrogen-evolution-reaction electrocatalysts, *J. Mater. Chem. A* 6 (2018) 19038–19046.
- [32] Z. Gao, F.Q. Liu, L. Wang, F. Luo, Hierarchical Ni₂P@NiFeAlO_x nanosheet arrays as bifunctional catalysts for superior overall water splitting, *Inorg. Chem.* 58 (2019) 3247–3255.
- [33] Z.-J. Chen, G.-X. Cao, L.-Y. Gan, H. Dai, N. Xu, M.-J. Zang, H.-B. Dai, H. Wu, P. Wang, Highly dispersed platinum on honeycomb-like NiO@Ni film as a synergistic electrocatalyst for the hydrogen evolution reaction, *ACS Catal.* 8 (2018) 8866–8872.
- [34] R. Boppella, J. Tan, W. Yang, J. Moon, Homologous CoP/NiCoP heterostructure on N-Doped carbon for highly efficient and pH-Universal hydrogen evolution electrocatalysis, *Adv. Funct. Mater.* 29 (2018) 1807976.
- [35] B. Wang, C. Tang, H.-F. Wang, X. Chen, R. Cao, Q. Zhang, A nanosized CoNi Hydroxide@Hydroxysulfide core-shell heterostructure for enhanced oxygen evolution, *Adv. Mater.* 31 (2019) 1805658.
- [36] T. Zhang, K. Yang, C. Wang, S. Li, Q. Zhang, X. Chang, J. Li, S. Li, S. Jia, J. Wang, L. Fu, Nanometric Ni₅P₄ clusters nested on NiCo₂O₄ for efficient hydrogen production via alkaline water electrolysis, *Adv. Energy Mater.* 8 (2018) 1801690.
- [37] I.K. Mishra, H. Zhou, J. Sun, K. Dahal, S. Chen, Z. Ren, Hierarchical CoP/Ni₅P₄/CoP microspheres arrays as a robust pH-universal electrocatalyst for efficient hydrogen generation, *Energy Environ. Sci.* 11 (2018) 2246–2252.
- [38] C.-C. Hou, Q. Li, C. Wang, C.-Y. Peng, Q.-Q. Chen, H.-F. Ye, W. Fu, C.-M. Che, N. Lopez, Ternary Ni-Co-P nanoparticles and their hybrids with graphene as noble-metal-free catalysts to boost the hydrolytic dehydrogenation of ammonia-borane, *Energy Environ. Sci.* 10 (2017) 1770–1776.
- [39] S.S. Williamson, P.A. Cassani, S. Lukic, B. Blunier, Chapter 6 - energy storage, in: M.H. Rashid (Ed.), *Alternative Energy in Power Electronics*, Butterworth-Heinemann, Boston, 2011, pp. 267–315.
- [40] C. Wu, J. Zhang, J. Guo, L. Sun, J. Ming, H. Dong, Y. Zhao, J. Tian, X. Yang, Ceria-induced strategy to tailor Pt atomic clusters on cobalt-nickel oxide and the synergistic effect for superior hydrogen generation, *ACS Sustain. Chem. Eng.* 6 (2018) 7451–7457.
- [41] Y. Shi, Y. Zhou, D.R. Yang, W.X. Xu, C. Wang, F.B. Wang, J.J. Xu, X.H. Xia, H.Y. Chen, Energy level engineering of MoS₂ by transition-metal doping for accelerating hydrogen evolution reaction, *J. Am. Chem. Soc.* 139 (2017) 15479–15485.
- [42] L. Cui, Y. Xu, L. Niu, W. Yang, J. Liu, Monolithically integrated CoP nanowire array: an on/off switch for effective on-demand hydrogen generation via hydrolysis of NaBH₄ and NH₃BH₃, *Nano Res.* 10 (2017) 595–604.
- [43] T. Liu, K. Wang, G. Du, A.M. Asiri, X. Sun, Self-supported CoP nanosheet arrays: a non-precious metal catalyst for efficient hydrogen generation from alkaline NaBH₄ solution, *J. Mater. Chem. A* 4 (2016) 13053–13057.
- [44] H.W. Liang, W. Wei, Z.S. Wu, X. Feng, K. Mullen, Mesoporous metal-nitrogen-doped carbon electrocatalysts for highly efficient oxygen reduction reaction, *J. Am. Chem. Soc.* 135 (2013) 16002–16005.
- [45] H. Tan, J. Tang, J. Henzie, Y. Li, X. Xu, T. Chen, Z. Wang, J. Wang, Y. Ide, Y. Bando, Y. Yamauchi, Assembly of hollow carbon nanospheres on graphene nanosheets and creation of iron-nitrogen-doped porous carbon for oxygen reduction, *ACS Nano* 12 (2018) 5674–5683.
- [46] L. Zhou, J. Meng, P. Li, Z. Tao, L. Mai, J. Chen, Ultrasmall cobalt nanoparticles supported on nitrogen-doped porous carbon nanowires for hydrogen evolution from ammonia borane, *Mater. Horiz.* 4 (2017) 268–273.
- [47] J. Jia, T. Xiong, L. Zhao, F. Wang, H. Liu, R. Hu, J. Zhou, W. Zhou, S. Chen, Ultrathin N-Doped Mo₂C nanosheets with exposed active sites as efficient electrocatalyst for hydrogen evolution reactions, *ACS Nano* 11 (2017) 12509–12518.
- [48] D.J. Li, U.N. Maiti, J. Lim, D.S. Choi, W.J. Lee, Y. Oh, G.Y. Lee, S.O. Kim, Molybdenum sulfide/N-doped CNT forest hybrid catalysts for high-performance hydrogen evolution reaction, *Nano Lett.* 14 (2014) 1228–1233.
- [49] X. Yang, A.-Y. Lu, Y. Zhu, M.N. Hedhili, S. Min, K.-W. Huang, Y. Han, L.-J. Li, CoP nanosheet assembly grown on carbon cloth: a highly efficient electrocatalyst for hydrogen generation, *Nano Energy* 15 (2015) 634–641.
- [50] S.K. Singh, V.M. Dhavale, S. Kurungot, Low surface energy plane exposed Co₃O₄ nanocubes supported on nitrogen-doped graphene as an electrocatalyst for efficient water oxidation, *ACS Appl. Mater. Interfaces* 7 (2014) 442–451.